Title
Imaging the Local Charge Environment of Nitrogen-Vacancy Centers in Diamond.

Journal
Physical review letters, 121(24)

ISSN
0031-9007

Authors
Mittiga, T
Hsieh, S
Zu, C
et al.

Publication Date
2018-12-01

DOI
10.1103/physrevlett.121.246402

Peer reviewed

Imaging the local charge environment of nitrogen-vacancy centers in diamond

T. Mittiga,[1,*] S. Hsieh,[1,2,*] C. Zu,[1,*] B. Kobrin,[1,2] F. Machado,[1] P. Bhattacharyya,[1,2]
N. Rui,[1] A. Jarmola,[1,3] S. Choi,[1] D. Budker,[4,1] and N. Y. Yao[1,2]

[1]*Department of Physics, University of California, Berkeley, CA 94720, USA*
[2]*Materials Science Division, Lawrence Berkeley National Laboratory, Berkeley, CA 94720, USA*
[3]*U.S. Army Research Laboratory, Adelphi, MD 20783, USA*
[4]*Helmholtz Institut, Johannes Gutenberg-Universität Mainz, 55099 Mainz, Germany*

Characterizing the local *internal* environment surrounding solid-state spin defects is crucial to harnessing them as nanoscale sensors of *external* fields. This is especially germane to the case of defect ensembles which can exhibit a complex interplay between interactions, internal fields and lattice strain. Working with the nitrogen-vacancy (NV) center in diamond, we demonstrate that local electric fields dominate the magnetic resonance behavior of NV ensembles at low magnetic field. We introduce a simple microscopic model that quantitatively captures the observed spectra for samples with NV concentrations spanning over two orders of magnitude. Motivated by this understanding, we propose and implement a novel method for the nanoscale localization of individual charges within the diamond lattice; our approach relies upon the fact that the charge induces an NV dark state which depends on the electric field orientation.

A tremendous amount of recent effort has focused on the creation and control of nanoscale defects in the solid-state [1, 2]. The spectral properties of these defects often depend sensitively on their environment. On the one hand, this sensitivity naturally suggests their use as nanoscale quantum sensors of *external* signals. On the other hand, accurately quantifying these signals requires the careful characterization of *internal* local fields. Here, we focus on a particular defect, the negatively charged nitrogen-vacancy (NV) color center in diamond [2, 3]. The electronic spin associated with the NV center is sensitive to a broad range of external signals, from magnetic and electric fields to pressure, temperature and gyroscopic precession [4–13]. Isolated single NVs have been used to explore phenomena in biology [2, 14–17], materials science [18–22], and fundamental physics [23–25].

More recently, many-body correlations have emerged as a powerful resource for enhancing the sensitivity of interacting spin ensembles [26–30]. To this end, a number of studies have explored and leveraged the properties of high-density NV systems [7, 31–38]. The local environment in such systems is substantially more complex than that of isolated NVs; this arises from a competition between multiple effects, including: lattice strain, paramagnetic impurities, charge dynamics, and NV-NV dipolar interactions. While the presence of an applied external magnetic field can suppress some of these effects, it significantly limits the scope of sensing applications such as zero-field nuclear magnetic resonance spectroscopy [39, 40]. Thus, characterizing and understanding the spectral properties of NV ensembles at zero field is crucial to utilizing these systems as quantum sensors.

In this Letter, we present three main results. First, we demonstrate that the characteristic splitting of the NV's magnetic resonance spectrum (Fig. 1a), observed in ensemble NV experiments [9, 15, 41–57], originates from its local electric environment; this contrasts with the conventional picture that strain dominates the zero-field properties of these systems. Second, we introduce

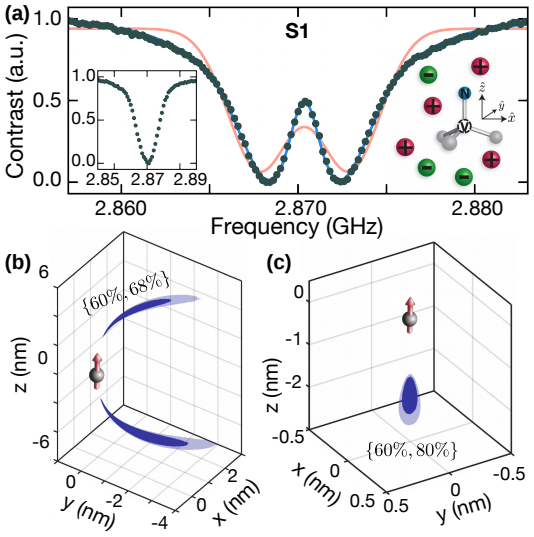

FIG. 1. Typical optically-detected magnetic resonance (ODMR) spectrum of an electron-irradiated and annealed Type-Ib diamond sample (S1) at zero magnetic field. The spectrum exhibits heavy tails which cannot be reproduced by either a double Lorentzian or Gaussian (orange fit) profile. The blue theory curve is obtained via our microscopic charge model. (Left inset) A typical zero-field spectrum for a single NV center shows only a single resonance. (Right inset) Schematic depicting an equal density of positive (e.g. N^+) and negative (e.g. NV) charges, which together, create a random local electric field at each NV center's position. (b) Nanoscale localization (∼5 nm) of a single positive charge via dark-state spectroscopy of an isolated NV center. The shaded regions indicate the probable location of the charge with darker indicating a higher likelihood. Percentages shown correspond to the confidence intervals of the dark/light region, respectively. (c) Analogous localization of a more proximal charge defect (∼2 nm) for a different NV center.

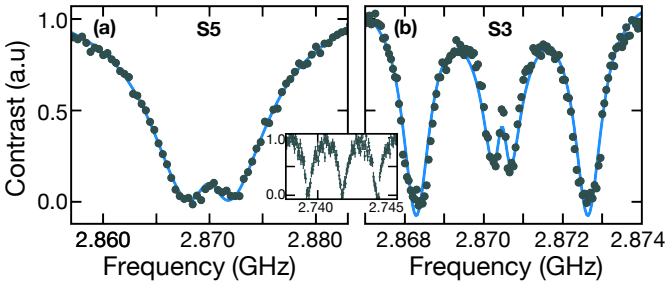

FIG. 2. ODMR spectra at zero magnetic field for (a) a Type-Ib untreated diamond sample (S5) and (b) a Type-IIa electron-irradiated and annealed sample (S3). The spectra portray the two qualitative regimes one expects based upon the average electric field strength as shown schematically in the right panel of Fig. 3d. The blue theory curve is obtained via our microscopic charge model. (inset) The spectrum for S3 at a magnetic field ≈ 45 G exhibits three identical hyperfine resonances.

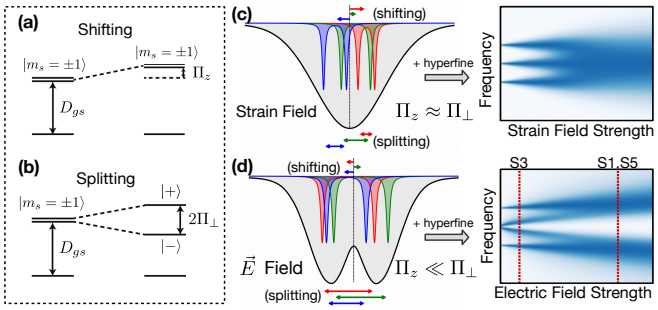

FIG. 3. Both strain and electric fields lead to (a) shifting Π_z and (b) splitting $2\Pi_\perp$ of the $|m_s = \pm 1\rangle$ manifold. (c) When averaged over an ensemble of NV centers, random local strain fields lead to a single broad spectral feature (at large strain). (d) In contrast, random local electric fields lead to two distinct spectral regimes: at small electric fields, the center hyperfine resonance splits, leading to a total of four resolvable features (S3); at large electric field, one obtains the characteristic split resonance seen in typical high density NV ensembles (S1, S5).

a charge-based model (Fig. 1a, right inset) that quantitatively reproduces the observed ODMR spectra for samples spanning two orders of magnitude in NV density. Third, our model suggests the ability to directly *image* the position of individual charges inside the diamond lattice. To this end, we propose and implement a novel method that localizes such charges to nanometer-size volumes (Fig. 1b,c). The essence of our approach is to leverage the interplay between the polarization of the applied microwave field and the orientation of the local electric field.

Magnetic spectra of NV ensembles—The NV center has a spin triplet ground state ($|m_s = \pm 1, 0\rangle$), which can be initialized and read out via optical excitation and coherently manipulated using microwave fields [58]. In the absence of any external perturbations, the $|m_s = \pm 1\rangle$ states are degenerate and separated from $|m_s = 0\rangle$ by $D_{\rm gs} = (2\pi) \times 2.87$ GHz (Fig. 3a).

This leads to the usual expectation of a single resonance peak at $D_{\rm gs}$, consistent with experimental observations of isolated NVs (Fig. 1a, inset). However, for high-density NV ensembles, one observes a qualitatively distinct spectrum, consisting of a pair of resonances centered at $D_{\rm gs}$ (Fig. 1a, sample S1). This spectrum poses a number of puzzles: First, the line-shape of each resonance is asymmetric and cannot be captured by either a Gaussian or Lorentzian profile. Second, the central feature between the resonances is sharper than the inhomogenous linewidth. Third, despite the presence of a strong *splitting*, there exists almost no *shift* of the NV's overall spectrum.

These generic features are present in diamond samples with NV and P1 (nitrogen impurity) densities spanning over two orders of magnitude. Fig. 2 demonstrates this ubiquity. In particular, it depicts the spectrum for two other samples: one with a significantly lower NV concentration (Fig. 2a, sample S5) and a second with significantly lower concentrations for both NVs and P1s (Fig. 2b, sample S3). In this latter case, the P1 density is low enough that the hyperfine interaction between the NV's electronic spin and its host ^{14}N nuclear spin can be resolved. Normally, this hyperfine splitting would simply result in three identical resonances split from one another by $A_{zz} = (2\pi) \times 2.16$ MHz [59] (Fig. 2, inset). However, as shown in Fig. 2b, one finds that the central hyperfine resonance is split in direct analogy to the prior spectra.

The most distinct of the aforementioned features – a split central resonance – has typically been attributed to the presence of lattice strain [9, 42–57]. Such strain can indeed lead to a coupling between the $|m_s = \pm 1\rangle$ states, and thus split their energy levels. However, a more careful analysis reveals an important inconsistency. In particular, given the measured strain susceptibility parameters [42], for each individual NV, any strain-induced splitting should be accompanied by a comparable shift of the overall spectrum (Fig. 3). Ensemble averaging then naturally leads to a spectrum that exhibits *only* a single broadened resonance (Fig. 3c).

Microscopic charge model—In contrast, we demonstrate that all of the observed features can be quantitatively explained via a microscopic model based upon randomly positioned charges inside the diamond lattice. The physical intuition underlying this model is simple: each (negatively charged) NV center plays the role of an electron acceptor, and charge neutrality implies that there must be a corresponding positively charged electron donor (typically thought to be N^+, a positively charged P1 center).

Such charges produce an electric field that also (like strain) couples the $|m_s = \pm 1\rangle$ states, leading to the splitting of the resulting eigenstates. Crucially, however,

Sample	ρ_c (ppm)	ρ_{NV} (ppm)	ρ_s (ppm)	Γ (MHz)
Ib treated (S1)	1.35(5)	1-10	70(5)	1.16(2)
Ib treated (S2)	1.7(1)	1-10	100(5)	0.78(3)
IIa treated (S3)	0.06(2)	0.01-0.1	12(3)	0.26(2)
Ib untreated (S4)	3.6(4)	0.001-0.01	90(20)	1.0(1)
Ib untreated (S5)	0.9(2)	0.001-0.01	130(30)	3.3(1)
IIa untreated (S6)	0.05(1)	0.001-0.01	16(2)	0.08(3)

TABLE I. Summary of the measured and extracted parameters for each diamond sample. ρ_c and Γ are directly extracted from our microscopic model, while ρ_s is independently measured at high magnetic fields and ρ_{NV} is estimated from fluorescence counts [64].

the NV's susceptibility to transverse electric fields (which cause splitting) is ∼50 times larger than its susceptibility to axial electric fields (which cause shifting) [60, 61]. This implies that even upon ensemble averaging, the electric-field-induced splitting remains prominent (Fig. 3d).

Qualitative picture in hand, let us now introduce the details of our microscopic model. In particular, we consider each NV to be surrounded by an equal density, ρ_c, of positive and negative charges [62]. These charges generate a local electric field at the position of the NV center and couple to its spin via the Hamiltonian:

$$H = (D_{gs} + \Pi_z)\, S_z^2 + (\delta B_z + A_{zz} I_z) S_z + \Pi_x (S_y^2 - S_x^2) + \Pi_y (S_x S_y + S_y S_x). \quad (1)$$

Here, $\hat{z}$ is the NV-axis, $\hat{x}$ is defined such that one of the carbon-vacancy bonds lies in the x-z plane (Fig. 1a, right inset), $\vec{S}$ are the electronic spin-1 operators of the NV, $\vec{I}$ are the nuclear spin-1 operators of the host ^{14}N [63], and δB_z represents a random local magnetic field (for example, generated by nearby paramagnetic impurities). Note that we absorb the gyromagnetic ratio into δB_z. The two terms $\Pi_{\{x,y\}} = d_\perp E_{\{x,y\}}$ and $\Pi_z = d_\parallel E_z$ characterize the NV's coupling to the electric field, $\vec{E}$, with susceptibilities $\{d_\parallel, d_\perp\} = \{0.35, 17\}$ Hz cm/V [60].

In order to obtain the spectra for a single NV, we sample $\vec{E}$ and δB_z from their random distributions and then diagonalize the Hamiltonian. Moreover, to account for the natural linewidth of each resonance, we include an additional Lorentzian broadening with full-width-half-maximum, Γ [64]. Averaging over this procedure yields the ensemble spectrum. The distribution of $\vec{E}$ is determined by the random positioning of the aforementioned charges. The distribution of δB_z is determined by the local magnetic environment, which depends sensitively on the concentration of spin defects (Table I).

In samples S1 and S5 (Type-Ib diamond), δB_z is dominated by the dipolar interaction with a high-density P1 spin bath, whose concentration, ρ_s, is independently characterized [64]. Meanwhile, in sample S3 (Type-IIa diamond), the P1 density is over two orders of magnitude smaller, leading to a δB_z that is dominated by interactions with ^{13}C nuclei (with a natural abundance of 1.1%); despite this difference in microscopic origin, one can also characterize the effect of this nuclear spin bath using an effective density, ρ_s [64]. For each sample, using this independently characterized ρ_s, we then fit the experimental spectrum by varying ρ_c and Γ . We find excellent agreement for all three samples (Fig. 1, 2) despite their vastly different defect concentrations (Table I).

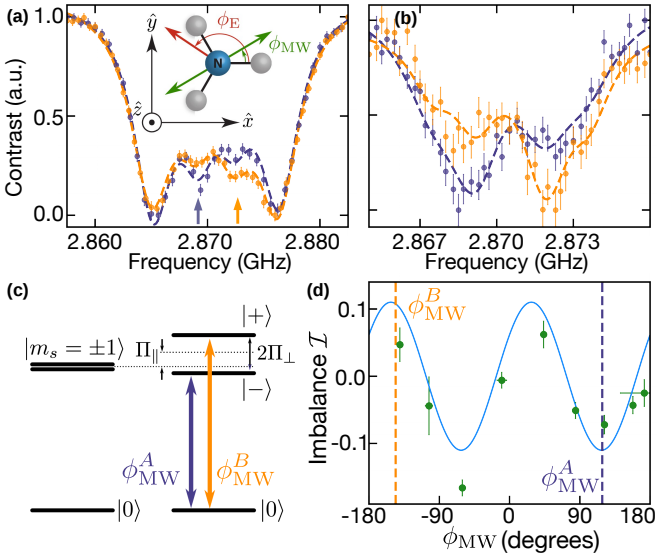

FIG. 4. Charge localization via dark-state spectroscopy. (a) Single NV ODMR spectra (untreated Type-Ib diamond) for two different microwave polarizations, ϕ_{MW}, depicting the reversal of the split-peak imbalance. The data correspond to the localized charge shown in Fig. 1b. (inset) Top view through the NV-axis ($\hat{z}$), where ϕ_E and ϕ_{MW} are defined with respect to $\hat{x}$ (along a carbon-vacancy bond). (b) Analogous split-peak imbalance data corresponding to the localized charge shown in Fig. 1c. (c) By changing the microwave polarization, ϕ_{MW}, one can directly control the coupling strength between the $|0\rangle$ and $|\pm\rangle$ states. (d) Measuring the change in the imbalance as a function of ϕ_{MW} allows one to extract the orientation of the electric field. Dashed lines indicate the polarizations plotted in (a).

A few remarks are in order. First, the presence of local electric fields suppresses the effect of magnetic noise when $\delta B_z \ll \Pi_\perp = \sqrt{\Pi_x^2 + \Pi_y^2}$. This is precisely the origin for both the sharpness of the inner central feature seen in Fig. 1a, as well as the narrowness of the inner hyperfine resonances seen in Fig. 2b. Second, in samples where the electric field dominates, the long-range, power-law nature of the electric field leads to a particularly heavy tailed spectrum [64]. Third, the extracted charge density, ρ_c, is consistent with the estimated NV density, ρ_{NV}, for all "treated" (electron-irradiated and annealed) samples (S1-S3). This agrees with our previous physical intuition: NVs behave as electron acceptors while P1s behave as electron donors. Interestingly, this

simple picture does not directly translate to "untreated" samples (S4-S6) where the observed charge density is significantly larger than ρ_{NV} (Table I); one possible explanation is that such samples harbor a higher density of non-NV charged defects (e.g. vacancy complexes [65]).

Nanoscale imaging of a single charge—Our microscopic model suggests that in samples where one can resolve single NV centers, it should be possible to directly probe the *local* charge environment. However, one expects a key difference in contrast to ensemble measurements: for a single NV, the electric field has a definite orientation with respect to the NV axes (Fig. 4a diagram).

Crucially, this orientation (namely, the angle, ϕ_E, in the NV's transverse plane) dictates the way in which the electric field mixes the original $|m_s = \pm 1\rangle$ states into bright and dark states:

$$|\pm\rangle = \frac{1}{\sqrt{2}}\left(|m_s = +1\rangle \mp e^{-i\phi_E}|m_s = -1\rangle\right). \quad (2)$$

Applying a linearly polarized microwave field will then drive transitions between the $|m_s = 0\rangle$ state and the $|\pm\rangle$ states. However, the relative strength of the two transitions depends on both ϕ_E and the polarization of the microwave field, ϕ_{MW} (Fig. 4c). Thus, one generally expects the measured amplitudes of the corresponding resonances to be different. These expectations are indeed borne out by the data (Fig. 4a,b) [66]. We note that this observed imbalance in the inner hyperfine resonances for a *single* NV is naturally averaged out in an ensemble measurement.

Our detailed understanding of this spectroscopy for a single NV suggests a novel method to extract the full vector electric field and to localize the position of the corresponding charge. In particular, by measuring the imbalance as a function of ϕ_{MW}, one can extract the electric field orientation, ϕ_E. More specifically, we define the imbalance, $\mathcal{I} \equiv \frac{A_+ - A_-}{A_+ + A_-}$, where $A_\pm$ are the amplitudes of the $|m_s = 0\rangle \leftrightarrow |\pm\rangle$ resonances and derive [64]:

$$\mathcal{I} \sim -\cos(2\phi_{MW} + \phi_E). \quad (3)$$

Thus, $\phi_E = 124(5)^\circ$ can be extracted as the phase offset in Fig. 4d. In combination with the observed splitting and shifting of the inner resonances, $\Pi_z = 30(50)$ kHz, $\Pi_\perp = 650(10)$ kHz, one can fully reconstruct the local electric field vector [64]. We do not observe any changes to this field over the course of the experiment (months) and find that it varies for different NV centers. This suggests that it originates from a stationary local charge environment. Moreover, charge neutrality and a low defect density suggest that the electric field is generated by a single positive charge, which we can then localize to within a nanoscale volume (Fig. 1b,c).

Summary and outlook—While it is abundantly asserted in the literature that the zero-field spectral features of NV ensembles owe to lattice strain, here, we demonstrate that such spectra are in fact dominated by the effect of local electric fields. Using a microscopic charge model, we quantitatively capture the magnetic resonance spectra of NV ensembles for defect concentrations spanning two orders of magnitude. Moreover, we introduce a method to image the spatial location of individual charges near a single NV center with nanoscale precision.

These results open the door to a number of intriguing future directions. First, although we observe charge densities that are consistent with the NV density in all treated samples (and thus consistent with a picture for charge neutrality), we find a deviation from this understanding for untreated samples which exhibit an anomalously large charge density. Further study is necessary to reveal the precise nature of these additional charges. Second, our results provide an improved understanding of NV ensembles at low magnetic fields; this is of particular relevance to the sensing of electric fields, lattice strain and gyroscopic precession, as well as to studies of magnetically sensitive quantum materials. Third, the charge-induced suppression of δB_z suggests the possibility of enhancing the NV's resilience to magnetic noise. Finally, understanding the local charge environment of single NV centers could provide insights into the optical spectral diffusion observed at low temperatures [67, 68].

We gratefully acknowledge the insights of and discussions with A. Blezynski-Jayich, B. Hausmann, J. Moore, P. Maurer, P. Kehayias, J. Choi, E. Demler, and M. Lukin. This work was supported as part of the Center for Novel Pathways to Quantum Coherence in Materials, an Energy Frontier Research Center funded by the U.S. Department of Energy, Office of Science, Basic Energy Sciences under Award #DE-AC02-05CH11231. SH acknowledges support by the National Science Foundation Graduate Research Fellowship under Grant No. DGE 1752814. AJ acknowledges support from the Army Research Laboratory under Cooperative Agreement No. W911NF-18-2-0037. SC acknowledges the Miller Institute for Basic Research in Science. DB acknowledges support by the EU FET-OPEN Flagship Project ASTERIQS (action #820394), the German Federal Ministry of Education and Research (BMBF) within the Quantumtechnologien program (FKZ 13N14439), and the DFG through the DIP program (FO 703/2-1).

---

* These authors contributed equally to this work

[1] I. Aharonovich, D. Englund, and M. Toth, Nature Photonics **10**, 631 (2016).

[2] R. Schirhagl, K. Chang, M. Loretz, and C. L. Degen, Annual Review of Physical Chemistry **65**, 83 (2014), pMID: 24274702, https://doi.org/10.1146/annurev-physchem-040513-103659.

[3] M. W. Doherty, N. B. Manson, P. Delaney, F. Jelezko,

J. Wrachtrup, and L. C. Hollenberg, Physics Reports **528**, 1 (2013).
[4] J. Maze, P. Stanwix, J. Hodges, S. Hong, J. Taylor, P. Cappellaro, L. Jiang, M. G. Dutt, E. Togan, A. Zibrov, *et al.*, Nature **455**, 644 (2008).
[5] H. Mamin, M. Kim, M. Sherwood, C. Rettner, K. Ohno, D. Awschalom, and D. Rugar, Science **339**, 557 (2013).
[6] D. Toyli, D. Christle, A. Alkauskas, B. Buckley, C. Van de Walle, and D. Awschalom, Physical Review X **2**, 031001 (2012).
[7] V. M. Acosta, E. Bauch, A. Jarmola, L. J. Zipp, M. P. Ledbetter, and D. Budker, Applied Physics Letters **97**, 174104 (2010).
[8] R. Epstein, F. Mendoza, Y. Kato, and D. Awschalom, Nature physics **1**, 94 (2005).
[9] F. Dolde, H. Fedder, M. W. Doherty, T. Nöbauer, F. Rempp, G. Balasubramanian, T. Wolf, F. Reinhard, L. C. L. Hollenberg, F. Jelezko, and J. Wrachtrup, Nature Physics **7**, 459 (2011).
[10] F. Dolde, M. W. Doherty, J. Michl, I. Jakobi, B. Naydenov, S. Pezzagna, J. Meijer, P. Neumann, F. Jelezko, N. B. Manson, and J. Wrachtrup, Physical Review Letters **112**, 097603 (2014).
[11] M. W. Doherty, V. V. Struzhkin, D. A. Simpson, L. P. McGuinness, Y. Meng, A. Stacey, T. J. Karle, R. J. Hemley, N. B. Manson, L. C. Hollenberg, *et al.*, Physical review letters **112**, 047601 (2014).
[12] M. P. Ledbetter, K. Jensen, R. Fischer, A. Jarmola, and D. Budker, Physical Review A **86**, 052116 (2012).
[13] A. Ajoy and P. Cappellaro, Physical Review A **86**, 062104 (2012).
[14] D. Le Sage, K. Arai, D. Glenn, S. DeVience, L. Pham, L. Rahn-Lee, M. Lukin, A. Yacoby, A. Komeili, and R. Walsworth, Nature **496**, 486 (2013).
[15] G. Kucsko, P. C. Maurer, N. Y. Yao, M. Kubo, H. J. Noh, P. K. Lo, H. Park, and M. D. Lukin, Nature **500**, 54 (2013).
[16] D. M. Toyli, F. Charles, D. J. Christle, V. V. Dobrovitski, and D. D. Awschalom, Proceedings of the National Academy of Sciences **110**, 8417 (2013).
[17] L. P. McGuinness, Y. Yan, A. Stacey, D. A. Simpson, L. T. Hall, D. Maclaurin, S. Prawer, P. Mulvaney, J. Wrachtrup, F. Caruso, R. E. Scholten, and L. C. L. Hollenberg, Nature Nanotechnology **6**, 358 EP (2011).
[18] A. Laraoui, H. Aycock-Rizzo, Y. Gao, X. Lu, E. Riedo, and C. A. Meriles, Nature Communications **6**, 8954 (2015).
[19] M. Pelliccione, A. Jenkins, P. Ovartchaiyapong, C. Reetz, E. Emmanouilidou, N. Ni, and A. C. B. Jayich, Nature nanotechnology **11**, 700 (2016).
[20] C. Du, T. Van der Sar, T. X. Zhou, P. Upadhyaya, F. Casola, H. Zhang, M. C. Onbasli, C. A. Ross, R. L. Walsworth, Y. Tserkovnyak, *et al.*, Science **357**, 195 (2017).
[21] Y. Dovzhenko, F. Casola, S. Schlotter, T. X. Zhou, F. Büttner, R. L. Walsworth, G. S. Beach, and A. Yacoby, arXiv preprint arXiv:1611.00673 (2016).
[22] I. Gross, W. Akhtar, V. Garcia, L. Martínez, S. Chouaieb, K. Garcia, C. Carrétéro, A. Barthélémy, P. Appel, P. Maletinsky, *et al.*, Nature **549**, 252 (2017).
[23] G. Waldherr, P. Neumann, S. Huelga, F. Jelezko, and J. Wrachtrup, Physical Review Letters **107**, 090401 (2011).
[24] H. Bernien, B. Hensen, W. Pfaff, G. Koolstra, M. Blok, L. Robledo, T. Taminiau, M. Markham, D. Twitchen, L. Childress, *et al.*, Nature **497**, 86 (2013).
[25] B. Hensen, H. Bernien, A. E. Dréau, A. Reiserer, N. Kalb, M. S. Blok, J. Ruitenberg, R. F. L. Vermeulen, R. N. Schouten, C. Abellán, W. Amaya, V. Pruneri, M. W. Mitchell, M. Markham, D. J. Twitchen, D. Elkouss, S. Wehner, T. H. Taminiau, and R. Hanson, Nature **526**, 682 (2015).
[26] W. Wasilewski, K. Jensen, H. Krauter, J. J. Renema, M. Balabas, and E. S. Polzik, Physical Review Letters **104**, 133601 (2010).
[27] S. Simmons, J. A. Jones, S. D. Karlen, A. Ardavan, and J. J. Morton, Physical Review A **82**, 022330 (2010).
[28] J. A. Jones, S. D. Karlen, J. Fitzsimons, A. Ardavan, S. C. Benjamin, G. A. D. Briggs, and J. J. Morton, Science **324**, 1166 (2009).
[29] P. Cappellaro and M. D. Lukin, Physical Review A **80**, 032311 (2009).
[30] S. Choi, N. Y. Yao, and M. D. Lukin, ArXiv e-prints (2018), arXiv:1801.00042 [quant-ph].
[31] V. M. Acosta, E. Bauch, M. P. Ledbetter, C. Santori, K. M. C. Fu, P. E. Barclay, R. G. Beausoleil, H. Linget, J. F. Roch, F. Treussart, S. Chemerisov, W. Gawlik, and D. Budker, Physical Review B **80**, 115202 (2009).
[32] S. Steinert, F. Dolde, P. Neumann, A. Aird, B. Naydenov, G. Balasubramanian, F. Jelezko, and J. Wrachtrup, Review of Scientific Instruments **81**, 043705 (2010).
[33] B. Maertz, A. Wijnheijmer, G. Fuchs, M. Nowakowski, and D. Awschalom, Applied Physics Letters **96**, 092504 (2010).
[34] P. L. Stanwix, L. M. Pham, J. R. Maze, D. Le Sage, T. K. Yeung, P. Cappellaro, P. R. Hemmer, A. Yacoby, M. D. Lukin, and R. L. Walsworth, Physical Review B **82**, 201201 (2010).
[35] L. M. Pham, D. Le Sage, P. L. Stanwix, T. K. Yeung, D. Glenn, A. Trifonov, P. Cappellaro, P. R. Hemmer, M. D. Lukin, H. Park, A. Yacoby, and R. L. Walsworth, New Journal of Physics **13**, 045021 (2011).
[36] A. Jarmola, V. M. Acosta, K. Jensen, S. Chemerisov, and D. Budker, Physical Review Letters **108**, 197601 (2012).
[37] N. Bar-Gill, L. M. Pham, A. Jarmola, D. Budker, and R. L. Walsworth, Nature Communications **4**, 1743 (2013).
[38] A. Jarmola, A. Berzins, J. Smits, K. Smits, J. Prikulis, F. Gahbauer, R. Ferber, D. Erts, M. Auzinsh, and D. Budker, Applied Physics Letters **107**, 242403 (2015).
[39] D. Weitekamp, A. Bielecki, D. Zax, K. Zilm, and A. Pines, Physical review letters **50**, 1807 (1983).
[40] A. M. Thayer and A. Pines, Accounts of Chemical Research **20**, 47 (2002).
[41] A. Gruber, A. Dräbenstedt, C. Tietz, L. Fleury, J. Wrachtrup, and C. von Borczyskowski, Science **276**, 2012 (1997).
[42] M. S. J. Barson, P. Peddibhotla, P. Ovartchaiyapong, K. Ganesan, R. L. Taylor, M. Gebert, Z. Mielens, B. Koslowski, D. A. Simpson, L. P. McGuinness, J. McCallum, S. Prawer, S. Onoda, T. Ohshima, A. C. B. Jayich, F. Jelezko, N. B. Manson, and M. W. Doherty, Nano Letters **17**, 1496 (2017).
[43] R. Igarashi, Y. Yoshinari, H. Yokota, T. Sugi, F. Sugihara, K. Ikeda, H. Sumiya, S. Tsuji, I. Mori, H. Tochio, Y. Harada, and M. Shirakawa, Nano Letters **12**, 5726 (2012).

[44] J. Forneris, S. Ditalia Tchernij, P. Traina, E. Moreva, N. Skukan, M. Jakšić, V. Grilj, L. Croin, G. Amato, I. P. Degiovanni, B. Naydenov, F. Jelezko, M. Genovese, and P. Olivero, ArXiv e-prints (2017), arXiv:1706.07935 [cond-mat.mtrl-sci].

[45] X. Zhu, Y. Matsuzaki, R. Amsüss, K. Kakuyanagi, T. Shimo-Oka, N. Mizuochi, K. Nemoto, K. Semba, W. J. Munro, and S. Saito, Nature Communications **5**, 3424 (2014).

[46] M. Simanovskaia, K. Jensen, A. Jarmola, K. Aulenbacher, N. Manson, and D. Budker, Phys. Rev. B **87**, 224106 (2013).

[47] V. M. Acosta, E. Bauch, M. P. Ledbetter, A. Waxman, L.-S. Bouchard, and D. Budker, Phys. Rev. Lett. **104**, 070801 (2010).

[48] Y. Kubo, F. R. Ong, P. Bertet, D. Vion, V. Jacques, D. Zheng, A. Dréau, J. F. Roch, A. Auffèves, F. Jelezko, J. Wrachtrup, M. F. Barthe, P. Bergonzo, and D. Esteve, Physical Review Letters **105**, 140502 (2010).

[49] N. D. Lai, D. Zheng, F. Jelezko, F. Treussart, and J.-F. Roch, Applied Physics Letters **95**, 133101 (2009), https://doi.org/10.1063/1.3238467.

[50] E. Bourgeois, A. Jarmola, P. Siyushev, M. Gulka, J. Hruby, F. Jelezko, D. Budker, and M. Nesladek, Nature Communications **6**, 8577 (2015).

[51] L. Rondin, J.-P. Tetienne, T. Hingant, J. F. Roch, P. Maletinsky, and V. Jacques, Reports on Progress in Physics **77**, 056503 (2014).

[52] P. Jamonneau, M. Lesik, J. P. Tetienne, I. Alvizu, L. Mayer, A. Dréau, S. Kosen, J.-F. Roch, S. Pezzagna, J. Meijer, T. Teraji, Y. Kubo, P. Bertet, J. R. Maze, and V. Jacques, Phys. Rev. B **93**, 024305 (2016).

[53] M. Simanovskaia, K. Jensen, A. Jarmola, K. Aulenbacher, N. Manson, and D. Budker, Phys. Rev. B **87**, 224106 (2013).

[54] Y. Matsuzaki, H. Morishita, T. Shimooka, T. Tashima, K. Kakuyanagi, K. Semba, W. J. Munro, H. Yamaguchi, N. Mizuochi, and S. Saito, Journal of Physics: Condensed Matter **28**, 275302 (2016).

[55] E. H. Chen, H. A. Clevenson, K. A. Johnson, L. M. Pham, D. R. Englund, P. R. Hemmer, and D. A. Braje, Phys. Rev. A **95**, 053417 (2017).

[56] A. O. Levchenko, V. V. Vasil'ev, S. A. Zibrov, A. S. Zibrov, A. V. Sivak, and I. V. Fedotov, Applied Physics Letters **106**, 102402 (2015), https://doi.org/10.1063/1.4913428.

[57] L. G. Steele, M. Lawson, M. Onyszczak, B. T. Bush, Z. Mei, A. P. Dioguardi, J. King, A. Parker, A. Pines, S. T. Weir, W. Evans, K. Visbeck, Y. K. Vohra, and N. J. Curro, Applied Physics Letters **111**, 221903 (2017).

[58] J. R. Maze, A. Gali, E. Togan, Y. Chu, A. Trifonov, E. Kaxiras, and M. D. Lukin, New Journal of Physics **13**, 025025 (2011).

[59] B. Smeltzer, L. Childress, and A. Gali, New Journal of Physics **13**, 025021 (2011).

[60] E. V. Oort and M. Glasbeek, Chemical Physics Letters **168**, 529 (1990).

[61] Kobrin et al., in preparation (2018).

[62] We assume that the charges are independently positioned in three dimensions.

[63] We note that the the hyperfine interaction in the Hamiltonian is obtained under the secular approximation.

[64] See Supplementary Material for detailed information.

[65] G. Davies, Nature **269**, 498 (1977).

[66] We measure the ODMR spectra of 68 single NV centers in an untreated Type-Ib sample, and find four that exhibit a significant electric-field-induced splitting with amplitude difference at zero magnetic field [64].

[67] Y. Chu, N. P. de Leon, B. J. Shields, B. Hausmann, R. Evans, E. Togan, M. J. Burek, M. Markham, A. Stacey, A. S. Zibrov, A. Yacoby, D. J. Twitchen, M. Loncar, H. Park, P. Maletinsky, and M. D. Lukin, Nano Letters **14**, 1982 (2014).

[68] F. Jelezko, I. Popa, A. Gruber, C. Tietz, J. Wrachtrup, A. Nizovtsev, and S. Kilin, Applied Physics Letters **81**, 2160 (2002).

Supplementary Material: Imaging the local charge environment of nitrogen-vacancy centers in diamond

T. Mittiga,* S. Hsieh,* C. Zu,* B. Kobrin, F. Machado, P. Bhattacharyya,
N. Rui, A. Jarmola, S. Choi, D. Budker, and N. Y. Yao

(Dated: September 7, 2018)

CONTENTS

MATERIALS AND METHODS

Sample details

The six diamond samples used in this work are all sourced from Element Six. Three of them have been treated (electron irradiation at Prism Gem and vacuum annealing) to increase NV density. The details are listed in Table I.

Sample name	Synthesis	[N] (ppm)	Electron irradiation dose	Energy (MeV)	Anneal temperature (°C)	Spectrum
Ib treated (S1)	HPHT	$\lesssim$200	2×10^{18} cm^{-2}	2	800	Fig. 5a, main text Fig. 1a
Ib treated (S2)	HPHT	$\lesssim$200	1×10^{17} cm^{-2}	14	400; 800; 1200	Fig 5b
IIa treated (S3)	CVD	$\lesssim 1$	1×10^{17} cm^{-2}	2	700; 875	Fig. 5c, main text Fig. 2a
Ib untreated (S4)	HPHT	$\lesssim$200	n/a	n/a	n/a	Fig. 6a
Ib untreated (S5)	HPHT	$\lesssim$200	n/a	n/a	n/a	Fig. 6b, main text Fig. 2b
IIa untreated (S6)	CVD	$\lesssim$1	n/a	n/a	n/a	Fig. 6c

TABLE I. Details of all samples shown in main and supplementary text. All samples are sourced from Element Six. [N] is specified by the manufacturer.

Experimental apparatus

We conduct single and ensemble NV measurements in a scanning confocal microscope equipped with controllable magnetic field and microwave delivery (Fig. 1). A 532 nm laser beam (Coherent Compass 315M) shuttered by an

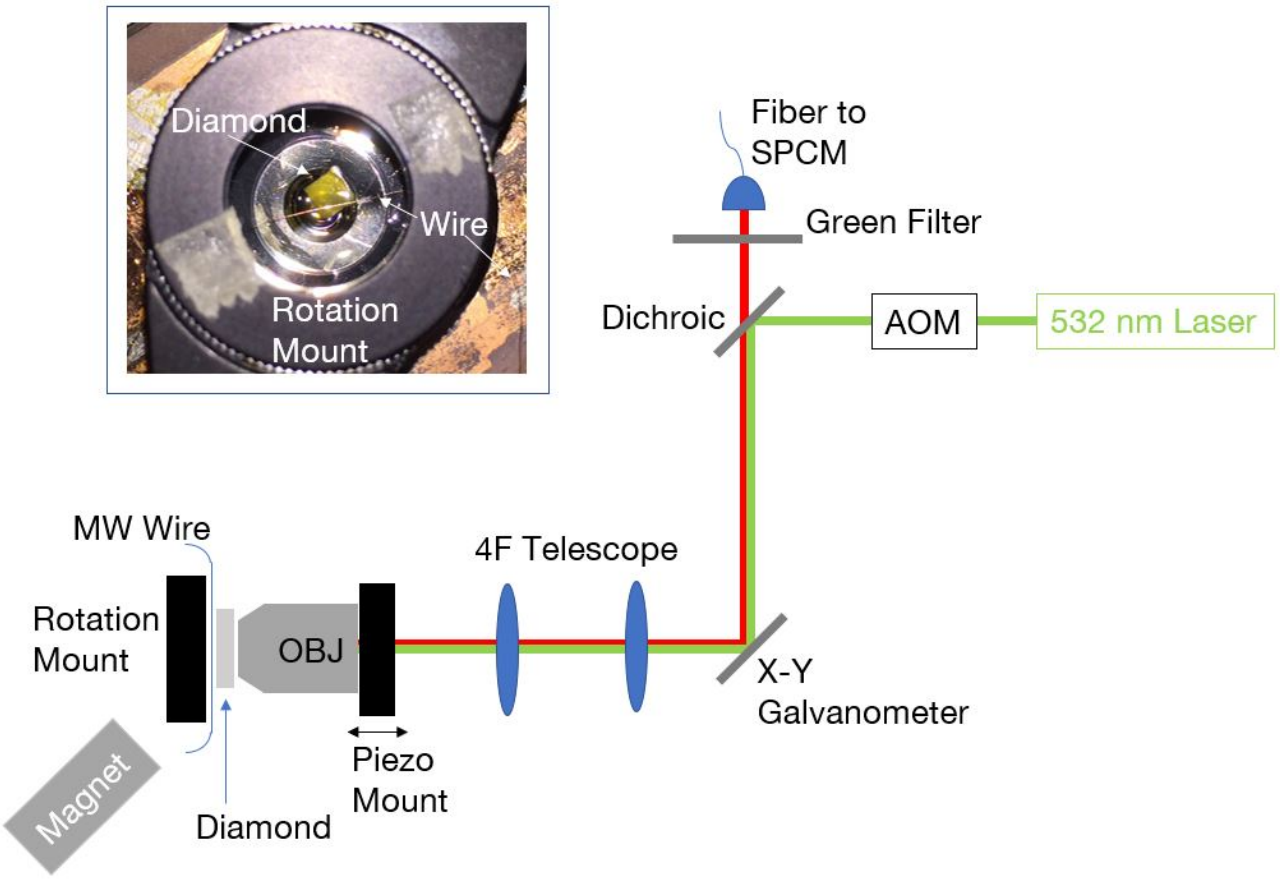

FIG. 1. Experimental Apparatus: A 532 nm laser shuttered by an AOM light switch excites the NVs, both for state preparation and read-out. A $4f$ telescope permits the galvonometer to scan the surface of the diamond and a piezo-mounted objective controls the depth of the focal plane. The objective lens focuses the excitation beam and collects fluorescence. Microwave fields are delivered by a magnet wire (as pictured) or a coplanar waveguide. Inset: Magnet wire stretched onto an optical rotation mount hovers over the surface of the diamond

acousto-optic modulator (AOM, Gooch & Housego AOMO 3110-120) is used for both ground state preparation and spin state detection. An objective lens focuses the beam to a diffraction limited spot size. We use an oil immersion objective lens (Nikon Plan Fluor 100x, NA 1.49) for resolving single NV centers or an air objective lens (Olympus LUCPLFLN, NA 0.6) for ensemble measurements. The combined action of an X-Y galvanometer (Thorlabs GVS212) and a $4f$ telescope provides the ability to scan the sample at the focal plane of the objective lens. A piezo mount for the objective lens serves to move the scanning plane in the longitudinal direction for depth scans.

The fluorescence photons collected by the objective lens are separated from the excitation beam path by a dichroic mirror (Semrock FF552-Di02). The coupling of the fluorescence beam to a single mode fiber serves as an effective pinhole for the confocal microscope. The fiber shuttles the fluorescence photons to a single photon counting module (SPCM, Excelitas SPCM-AQRH-64-FC) or avalanche photodiode (Thorlabs APD410A). We use a Data Aquisition card (DAQ) for fluorescence measurements and subsequent data processing (National Instruments USB 6343).

A microwave source (Stanford Research Systems SG384) in combination with a 16W amplifier (Mini-Circuits ZHL-16W-43+) serves to generate signals for spin state manipulation. For ensemble measurements, microwave signals are delivered using a coplanar waveguide (CPW) deposited on a coverslip. For single NV experiments, a 46 AWG magnet wire taped to a rotation mount (Thorlabs RSP05) is used (Fig. 1 inset). The magnet wire is adjusted to sit parallel to, and approximately 550 μm above, the focal plane of the objective lens. By rotating

the wire using the mount, we effectively change the polarization of the microwaves at the site of the single NV center of interest. The calculation of the polarization angle in the NV center frame is discussed later in the Section **Microwave Angle Projection**.

Pulse sequence for measuring magnetic resonance spectra of NVs

To measure the optically detected magnetic resonance (ODMR) spectra of NVs, we first use a 10 μs 532 nm laser pulse to initialize the spin triplet ground states to $m_s = 0$ (Fig. 2). After turning off the laser for 1 μs to allow the excited state population to decay, we apply a microwave π pulse and sweep its frequency. Our π pulse length is chosen as 2-6 μs for measurements on Type-Ib diamonds and 8-10 μs for Type-IIa diamonds to avoid power broadening. At the end, we apply another 10 μs laser pulse to detect the NV spin state by collecting the resulting fluorescence photons (Signal). In addition, we collect the photon counts at the end of the initialization laser pulse (Reference), and normalize the measured contrast.

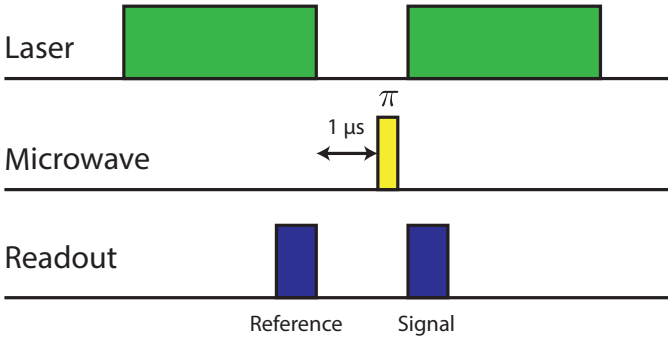

FIG. 2. Pulse sequence for ODMR measurement.

Isolating single NVs

The diamond sample used for single NV experiments is sample S4 (untreated type Ib). We found a region of the sample where we could isolate single NVs as confirmed by a $g^{(2)}$ measurement (Fig. 3).

CHARGE MODEL AND ENSEMBLE SPECTRUM

In this section, we provide additional details regarding our charge model. This includes an analysis of the electric and magnetic field distributions, as well as an explanation of the fitting procedure of the ensemble spectra and the estimation of error bars.

Electric field distribution

In our model, we consider each NV to be surrounded by an equal density, ρ_c of positive and negative point-like charges. We simulate the positions of these charges by randomly placing a large number ($N_{\text{charge}} \sim 100$) of points within a spherical volume. The radius of the sphere, R, is determined such that the average density of the charges matches ρ_{c}; in particular, this implies

$$R = \left(\frac{3}{4\pi} \frac{N_{\text{charge}}}{n_0 \rho_{\text{c}}} \right)^{\frac{1}{3}} \tag{1}$$

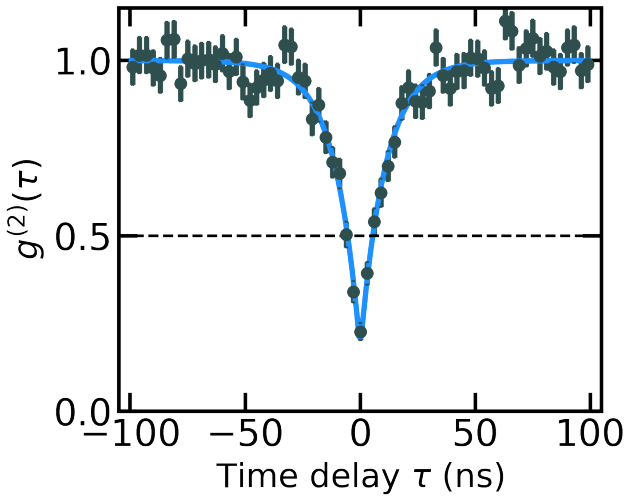

FIG. 3. $g^2(\tau)$ measurement on NV1: the extracted $g^2(0) = 0.17^{+0.05}_{-0.03} < 0.5$ definitively confirms it is a single NV center.

where $n_0 = 1.76 \times 10^{-4}$ (ppm·nm^3)$^{-1}$ is the factor relating the number density (in ppm) to the volume density. Based on the positions of the charges $\{\vec{r}_i\}$, we calculate the electric field at the center of the sphere (the NV's location):

$$\vec{E} = \sum_i \frac{e}{4\pi\epsilon_0\epsilon_r} \frac{\hat{r}_i}{r_i^2} \tag{2}$$

where $\epsilon_r = 5.7$ is the relative permittivity of diamond[1].

Sampling over $\{\vec{r}_i\}$ yields a distribution for $\vec{E}$. We are particularly interested in the transverse component, $E_\perp$, which couples ~ 50 times stronger to the NV, i.e. $\Pi_\perp = d_\perp E_\perp$. The distribution $P(\Pi_\perp)$ for various densities are shown in Fig. 4. We note that these distributions are related to each other by a simple rescaling, $\Pi_\perp \to \rho_c^{2/3}\Pi_\perp$, though we do not incorporate this rescaling explicitly in our sampling procedure.

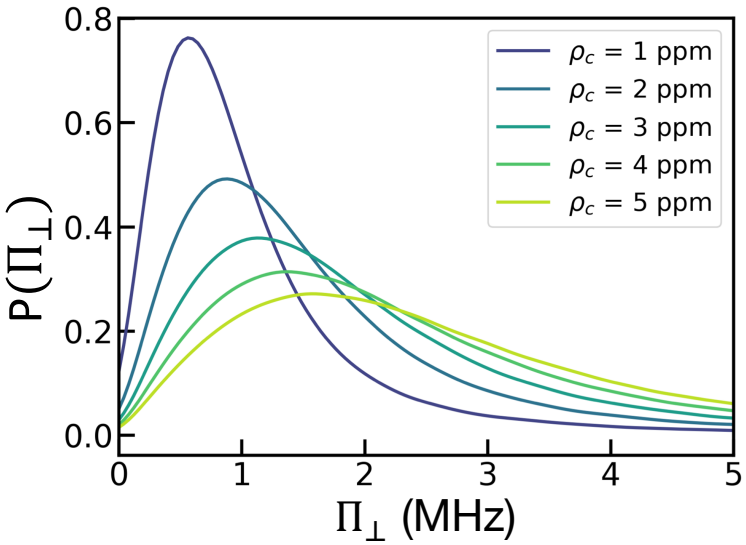

FIG. 4. Distributions for the transverse electric field component, $\Pi_\perp = d_\perp E_\perp$, at various charge densities. The distributions were generated by the charge sampling procedure described in the text.

Magnetic field distribution

We assume that the local magnetic environment arises from interactions with other magnetic impurities. For Type-Ib diamond, the dominant impurities are the electronic spins associated with P1 centers. For Type-IIa diamond, the leading contribution comes from the nuclear spins associated with ^{13}C (1.1% natural abundance).

In both cases, we model the effect of the magnetic impurities as a dipolar interaction between the NV and a bath of electronic spins $\left(s = \frac{1}{2}\right)$ at density ρ_{s}:

$$H_{\mathrm{dipolar}} = \sum_i -\frac{J_0}{r_i^3}\left(3(\hat{S}\cdot\hat{r}_i)(\hat{P}_i\cdot\hat{r}_i) - \hat{S}\cdot\hat{P}_i\right). \tag{3}$$

Here $\{\vec{r}_i\}$ are the positions of the magnetic impurities, $\hat{S}$, $\hat{P}_i$ are the spin operators for the NV and impurities, respectively, and $J_0 = (2\pi)52$ MHz·nm^3. Under the secular approximation, this interaction further simplifies to:

$$H_{\mathrm{dipolar}} = \delta B_z\ S_z \quad , \quad \delta B_z = \sum_i -\frac{J_0}{r_i^3}\left(3\hat{n}_i^z - 1\right)p_i\ , \tag{4}$$

where $\hat{n}_i^z = \hat{z}\cdot\hat{r}_i$, and $p_i = \pm 1/2$ are the spins of the magnetic impurities at the mean-field level.

A few remarks are in order. First, the coupling strength for nuclear spins is ~ 2600 times weaker. This can be effectively modeled by an electronic spin bath, whose the density is reduced by the same factor. All samples are then characterized with a single parameter ρ_{s}. Second, the ^{13}C nuclear spins give rise to an additional interaction via the Fermi contact term [2]. Because directly accounting for this is difficult, we approximate its effect as an extra contribution to ρ_{s}. The resulting spectra are in quantitative agreement with the experimental data at high field (Fig. 5,6), validating this approximation.

Similar to the electric field distribution, we sample $\{\vec{r}_i\}$ for $N_{spin} \sim 100$ from a sphere whose radius is chosen to be consistent with ρ_{s} (Eq. 1). In this case, we also sample a configuration of spins $\{p_i\}$ from a uniform distribution. Inserting $\{\vec{r}_i\}$ and ρ_{s} into Eq. 4 allows us to calculate δB_z for each realization.

Fitting procedure and error estimation

Our fitting procedure for each ensemble sample consists of two steps. First, we fit a spectrum taken at high magnetic field, where the effects of electric fields are highly suppressed and the dominant broadening is due to magnetic impurities (Figs. 5 and 6, left column). This allows us to characterize ρ_{s} independently. Second, we fit a spectrum at zero applied field using the previously determined magnetic noise and an additional contribution due to electric fields (Figs. 5 and 6, right column). This determines the charge density ρ_{c}, as well the the natural linewidth Γ.

For the high-field spectra, we sample over the magnetic impurities configurations following the procedure outlined in the previous section. For each configuration, we calculate the NV's resonance frequencies using the full Hamiltonian of the system, Eq. (1) of the main text. Repeating this procedure for ~ 5000 realizations, we obtain a histogram of resonance energies that is proportional to the experimentally observed spectra. We generate such spectra for a range of ρ_{s} and fit each individually to the high-field measurement, optimizing with respect to the center frequency, vertical offset, and overall amplitude. We characterize ρ_{s} by calculating the least-square residuals between our simulated spectra and the experimental data (Figs. 5 and 6, left column). In particular, we identify ρ_{s} that minimizes the residual as the best-fit parameter and estimate its error from the range of values whose residuals lie within 10% of the minimum.

The fitting procedure for the zero-field spectra follows in close analogy, except we now average over both the charge distribution and the magnetic impurity distribution. Specifically, we first sample the positions of the charges and calculate the electric field at the NV center (~ 5000 realizations). For each charge realization, we then sample over many configurations of magnetic impurities to simulate the magnetic noise (additional ~ 5000 realizations). Another important difference from before is that we now incorporate a natural linewidth for each resonance. To do so, we convolve the distribution of resonance frequencies with a Lorentzian profile characterized by a full-width-half-maximum Γ. This linewidth accounts for broadening that is independent from the charge environment or static magnetic fields. For example, it would include contributions from power broadening, fluctuating fields in the environment (i.e. $T_{2,\mathrm{echo}}$), and strain-induced broadening.

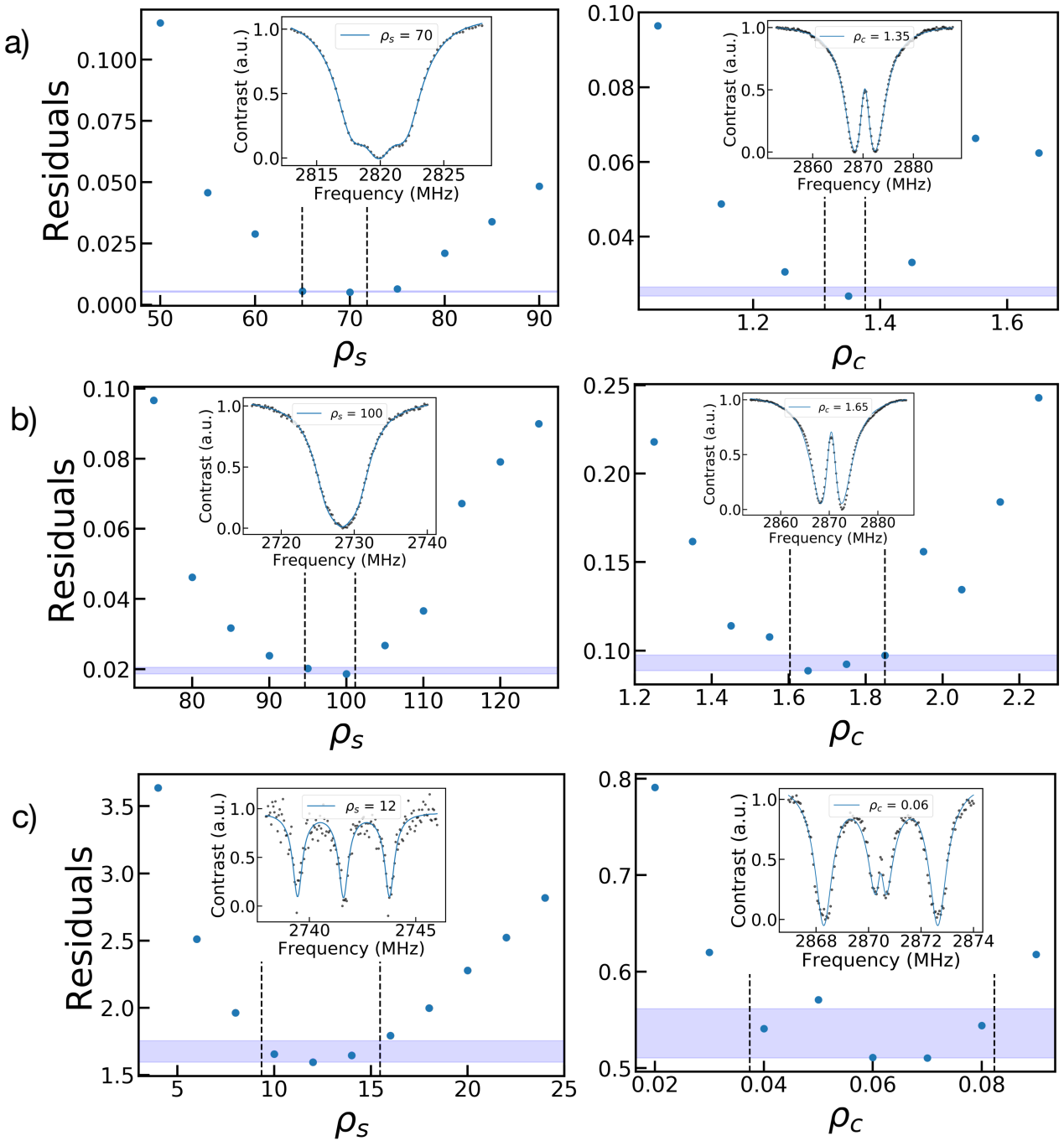

FIG. 5. Ensemble fitting procedure applied to the treated samples: (a) Ib treated (S1), (b) Ib treated (S2), and (c) IIa treated (S3). The main plots show the least-square residuals as a function of ρ_s (left) and ρ_c (right) under large ($\sim$ 25-50 G) and zero applied field, respectively. We identify the best-fit values for ρ_s, ρ_c based on the minimum residual, and we estimate their error from the range values whose residuals lie within 10% of the minimum (blue shaded regions). The insets depict the best-fit spectra (blue curve), along with the experimental data (black points).

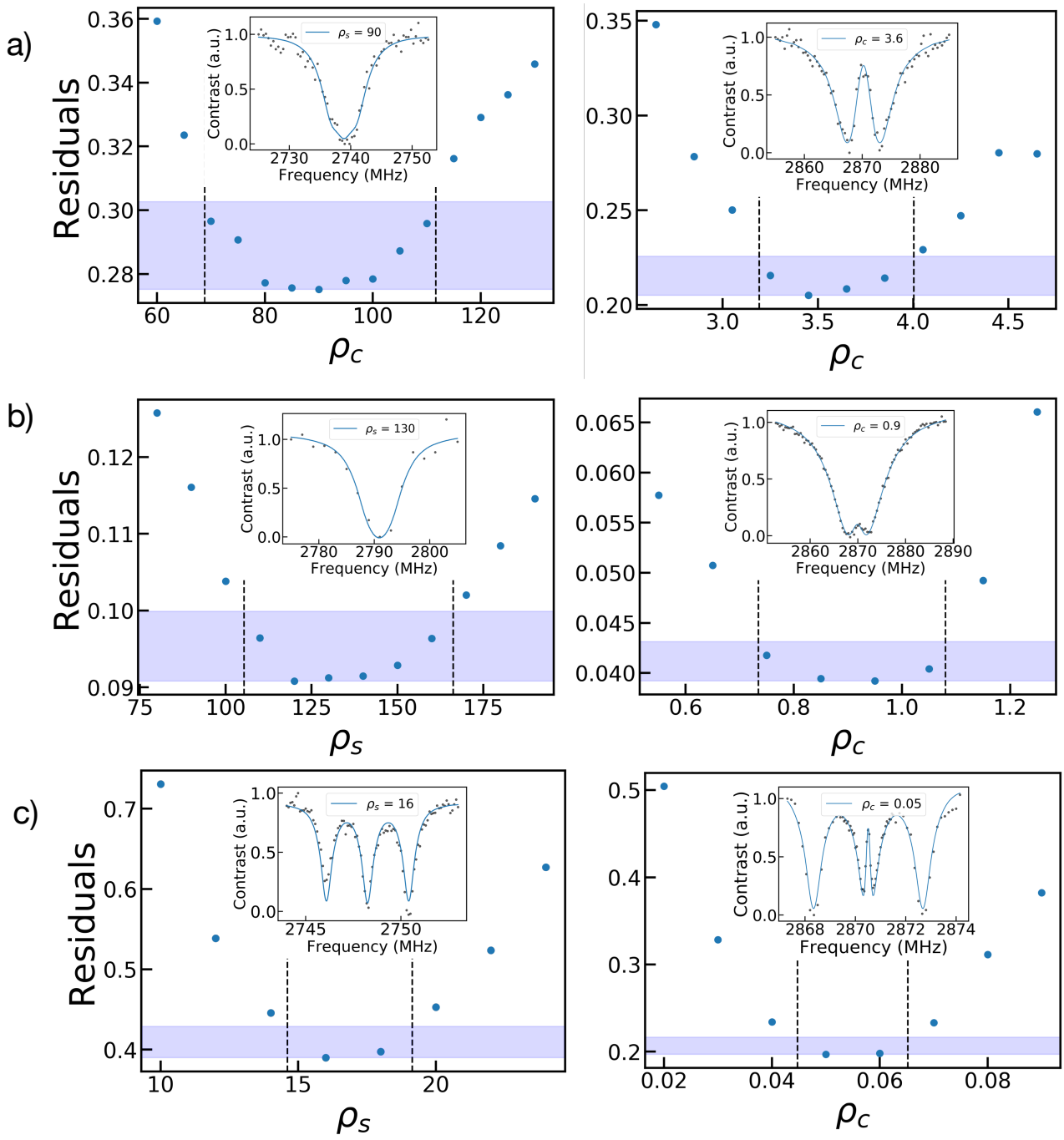

FIG. 6. Fitting procedure applied to the untreated samples: (a) Ib untreated (S4), (b) Ib untreated (S5), and (c) IIa treated (S6). See caption of Fig. 5 for description.

To isolate the effects due to the charge environment, we fit the zero-field spectra as a function of ρ_c while fixing the magnetic noise (ρ_s) based on the previous step. For each value of ρ_c, we optimize with respect to the natural linewidth Γ, the center frequency, overall amplitude, and vertical offset. These results are shown in the right column of Figs. 5 and 6. As before, we estimate the error on ρ_c from the 10% interval of the residuals, while for Γ we take the standard error estimated by the fitting routine.

All simulated spectra agree quantitatively with the experimental data, and the extracted ρ_s, ρ_c and Γ are listed

in Table I in the main text. We note that for one of the six samples (S5), the linewidth contribution from δB_z is on the same order as Γ. Since we assume δB_z is the dominant source of noise in the high field spectra when extracting ρ_s, the magnetic impurity density for this sample may not be precise.

CHARGE LOCALIZATION USING SINGLE NVS

In this section, we discuss the details associated with the charge localization based on a single NV. We consider the derivation of the imbalance and relate it to the electric field orientation and the microwave polarization. We note that the imbalance of the resonances is strong evidence for the presence of a nearby charge, as most other interactions would not modify the transition amplitudes differentially with respect to linearly polarized microwave fields.

To extract the position of the charge, we first calculate the polarization of the microwave field in the reference frame of the NV, ϕ_{MW} (Fig. 4a inset of the main text). By varying ϕ_{MW}, and measuring the imbalance one can directly extract the transverse orientation of the electric field ϕ_E. Combined with the observed splitting $2\Pi_\perp$ and shifting Π_z we can fully determine the local electric field vector and localize the corresponding charge. These procedures are detailed below.

Derivation of the Imbalance

In order to quantitatively extract the orientation of the electric field ϕ_E, we introduce the notion of imbalance as the difference in the weights of the resonances in the observed spectra. This imbalance $\mathcal{I}$ is directly related to ϕ_{MW} and the transverse orientation of the electric field ϕ_E.

We begin by focusing our attention to the states with ^{14}N nuclear spin $m_I = 0$ (two inner resonances). In the presence of an electric field, these states are described by the Hamiltonian:

$$H = (D_{gs} + \Pi_z)S_z^2 + \Pi_x(S_y^2 - S_x^2) + \Pi_y(S_xS_y + S_yS_x). \tag{5}$$

One finds that the electric field couples only the $|m_s = \pm 1\rangle$ states, leading to the new eigenstates:

$$|+\rangle = \frac{1}{\sqrt{2}}\left(|m_s = +1\rangle - e^{-i\phi_E}|m_s = -1\rangle\right) \tag{6}$$

$$|-\rangle = \frac{1}{\sqrt{2}}\left(e^{i\phi_E}|m_s = +1\rangle + |m_s = -1\rangle\right) \tag{7}$$

with energy splitting $2\Pi_\perp = 2\sqrt{\Pi_x^2 + \Pi_y^2}$.

The magnetic resonance spectrum is obtained by driving transitions from the $|m_s = 0\rangle$ state to the $|\pm\rangle$ states using a linearly polarized microwave field. The matrix elements associated with these transitions are

$$\mathcal{M}_\pm = \langle 0|\, S_x\cos\phi_{\mathrm{MW}} + S_y\sin\phi_{\mathrm{MW}}\,|\pm\rangle \tag{8}$$

$$= \frac{1}{2}\left[e^{-i\phi_{\mathrm{MW}}} \mp e^{i(\phi_E+\phi_{\mathrm{MW}})}\right] \tag{9}$$

where ϕ_{MW} is the direction of microwave polarization. This results in two resonances with amplitudes, $A_\pm \equiv |\mathcal{M}_\pm|^2$:

$$A_\pm = \frac{1}{2} \mp \frac{1}{2}\cos(2\phi_{\mathrm{MW}} + \phi_E). \tag{10}$$

By defining the imbalance $\mathcal{I} \equiv \frac{A_+ - A_-}{A_+ + A_-}$, we recover Eq. (2) in the main text:

$$\mathcal{I} = -\cos(2\phi_{\mathrm{MW}} + \phi_E). \tag{11}$$

We note that the imbalance reverses direction for $\phi_{\mathrm{MW}} \to \phi_{\mathrm{MW}} + 90^\circ$ and that, for certain microwave angles, the amplitude of one resonance can fully vanish.

For completeness, we also derive the imbalance of the outer ^{14}N hyperfine states, which correspond to $m_I = \pm 1$. The derivation follows the same logic as above, except the Hamiltonian is now

$$H = (D_{gs} + \Pi_z)S_z^2 + \Pi_x(S_y^2 - S_x^2) + \Pi_y(S_xS_y + S_yS_x) \pm 2A_{zz}S_z. \tag{12}$$

The eigenstates $|\pm\rangle$ are split by $2\sqrt{A_{zz}^2 + \Pi_\perp^2}$. For $m_I = 1$, one finds

$$|+\rangle = \frac{1}{\sqrt{1+\xi^2}}\left(|+1\rangle - \xi e^{-i\phi_E}|-1\rangle\right) \tag{13}$$

$$|-\rangle = \frac{1}{\sqrt{1+\xi^2}}\left(\xi e^{i\phi_E}|+1\rangle + |-1\rangle\right) \tag{14}$$

where

$$\xi = \frac{A_{zz}}{\Pi_\perp}\left(\sqrt{1+\left(\frac{\Pi_\perp}{A_{zz}}\right)^2} - 1\right) \tag{15}$$

An analogous expression holds for $m_I = -1$. In both cases, the amplitudes of the $|m_s = 0\rangle \leftrightarrow |\pm\rangle$ resonances are

$$A_\pm = \frac{1}{\sqrt{1+\xi^2}}\left(1 + \xi^2 \mp 2\xi\cos(2\phi_{\mathrm{MW}} + \phi_E)\right). \tag{16}$$

This leads to an imbalance:

$$\mathcal{I} = \frac{-2\xi\cos(2\phi_{\mathrm{MW}} + \phi_E)}{1+\xi^2}. \tag{17}$$

Thus, the imbalance of the outer resonances follows the same phase dependence as the inner resonances, but the maximum imbalance depends on the ratio $\Pi_\perp/A_{zz}$. In particular, in the limit $\Pi_\perp \gg A_{zz}$, $\xi \approx 1$ and a fully dark state is still possible; whereas, for $\Pi_\perp \ll A_{zz}$, the maximum imbalance is reduced to $\mathcal{I}_{\max} \approx \Pi_\perp/A_{zz}$.

The resulting dependence on ϕ_{MW} and ϕ_E does not change if we include the interaction with a nearby ^{13}C (within the secular approximation), since it interacts with the NV in a similar fashion to ^{14}N hyperfine.

Microwave Angle Projection

We define $(\hat{X}, \hat{Y}, \hat{Z})$ as our lab frame shown in Fig. 7a and the NV frame $(\hat{x}, \hat{y}, \hat{z})$ as shown in Fig. 1a left inset in the main text. These two frames are related by the crystallographic axes of the sample. We approximate the microwave delivery wire to be infinitely long, with an angle ϕ_{Wire} with respect to $\hat{X}$, and an in-plane distance r away from the NV. We extract ϕ_{Wire} and r from an image of the sample geometry (Fig. 1 inset). The height h of the wires plane above the NV is assumed to be 550 ± 100 μm given the thickness of the diamond 500 μm, the wire diameter 40 μm, and an intentional air gap to avoid contact to the sample (~ 30 μm). The wire carries a current which generates a linearly polarized microwave field at the location of the NV (Fig. 7) whose transverse projection ϕ_{MW} drives the $|m_s = 0\rangle \leftrightarrow |\pm\rangle$ transition. ϕ_{MW} is fully determined by the values $\{\phi_{\mathrm{Wire}}, h, r\}$. To estimate error in each realization of ϕ_{Wire}, we use a Monte Carlo method assuming a $\pm 10^\circ$ tilting of the wire out of the plane.

Single Charge Localization

We search through 68 single NVs and find four exhibiting a significant imbalance in the zero-field spectrum consistent with a nearby charge, from which we analyze two in this work (referred to as NV1 and NV2). Because these spectra can also be affected by the presence of a nearby strongly-coupled ^{13}C, we apply a bias B_z field, which suppresses the effect of the electric field and identifies the source of the splitting. The zero- and high-field spectra for these two NVs are shown in Fig. 8. For NV1, we find three resonances spaced $\sim$2.16 MHz apart, a signal associated exclusively with ^{14}N hyperfine. In contrast, for NV2 we observe four resonances, indicating the

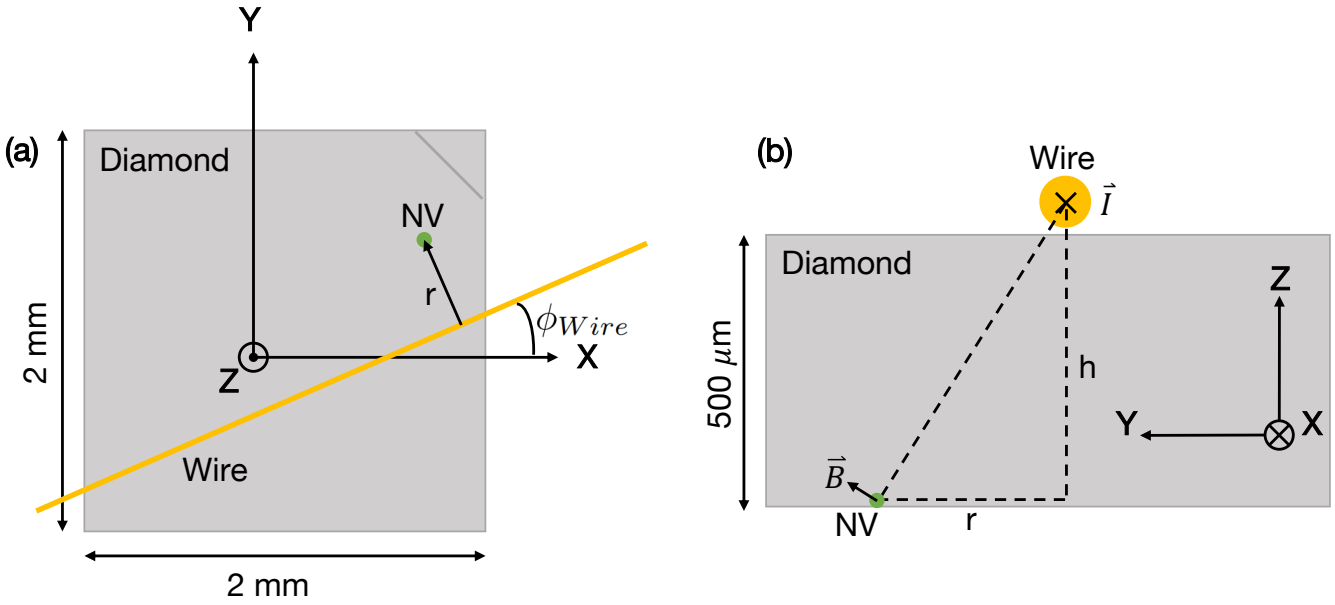

FIG. 7. a) Top view of lab frame, $\hat{X}$, $\hat{Y}$, and $\hat{Z}$ axes are defined as shown. Wire is displayed at an angle ϕ_{Wire} relative to X, and r is the distance between the wire and the NV. b) Side view of lab frame. With $\phi_{\text{Wire}} = 0$, when the oscillating current $\vec{I}$ flows in the direction shown, we calculate the direction of the magnetic field vector $\vec{B}$ at a height h below the wire as shown.

additional presence of a strongly-coupled ^{13}C. We fit the spectrum of NV2 to extract the ^{13}C hyperfine coupling strength $\approx 1.65(7)$ MHz. To confirm the charge origin, we then measure the full imbalance curve using dark-state spectroscopy.

For NV1, we can clearly resolve the four resonances. The information about the imbalance is encoded into the amplitude of the inner two resonances. To estimate these amplitudes we measure only six spectral data points for each ϕ_{MW} (Fig. 9): two data points closely spaced at the location of each of the two inner resonances and two data points far from the resonances (measurement of the baseline contrast) . The imbalance extracted with this method is shown in the main text Fig. 4d, from which we extract $\phi_E = 124(5)^\circ$.

For NV2, since we cannot clearly resolve the four resonances due to the presence of the nearby ^{13}C, we estimate imbalance by integrating the area on either side of the fit center frequency (Fig. 10 a). The imbalance curve is shown in Fig. 10b, from which we extract $\phi_E = 236(15)^\circ$.

We note that the amplitudes of these curves are much smaller than unity. This discrepancy from our simple theoretical model can also be explained by a few possibilities. First, our methods do not directly probe the weight of the transitions. Second, due to the intrinsic linewidth and power broadening, the inner and outer resonances overlap, which precludes isolating any single transition. Third, a dynamic charge bath may generate a background spectrum that is not included in our model.

In order to localize the charge, we also need to extract the charge-induced splitting $\Pi_\perp$ and shifting Π_z. In direct analogy to the treatment of ensembles, we fit the full zero-field single NV spectra using our microscopic model to extract these parameters as follows:

1. The spectra depend on five physical parameters: the three components of the electric field $\vec{E}$, the density of magnetic defects ρ_s, and the natural linewidth Γ. We also include a global amplitude scaling factor and background offset.

2. To account for the magnetic noise distribution, we follow a prescription similar to the previous magnetic field distribution section. We begin by considering the distribution of magnetic field for ρ_s which yields a probability distribution for measuring a particular value of δB_z. We then discretize over δB_z and for each possible value, perform steps 3-5. Each of the resulting spectra is weighted by the probability of measuring δB_z.

3. We solve the full Hamiltonian of the system (including ^{13}C and ^{14}N hyperfine interactions where applicable)

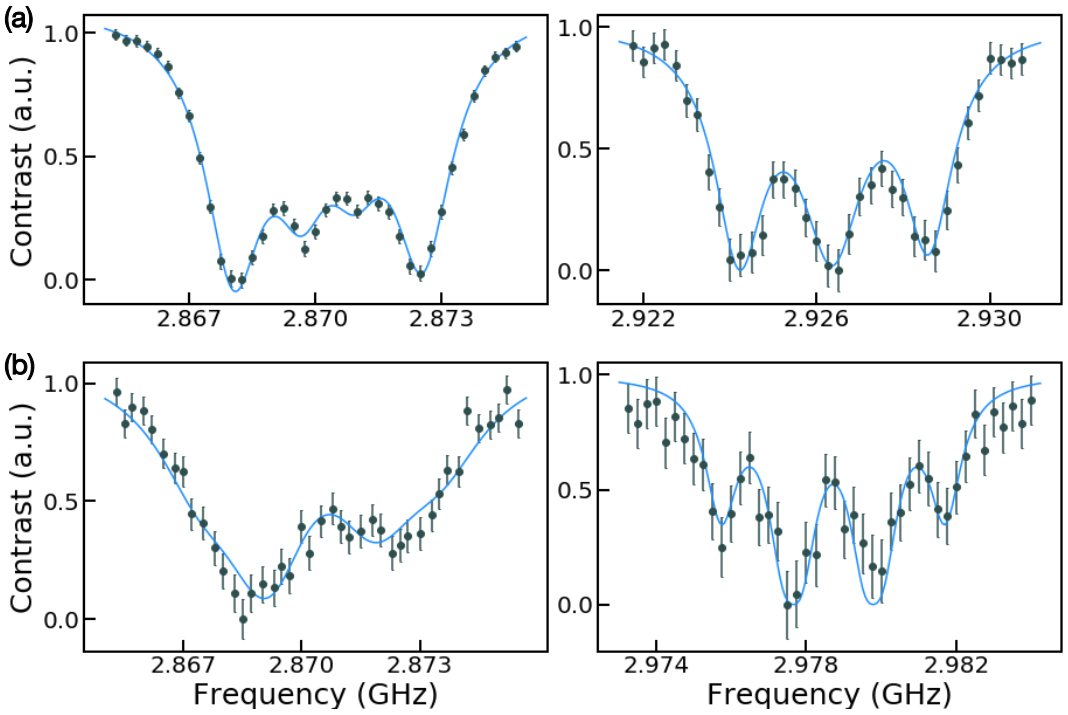

FIG. 8. Spectra taken with and without a magnetic field applied along the NV z-axis. a) Left: zero-field spectrum for NV1 with microscopic model fit; Right: spectrum with an applied magnetic field and a fit to 3 Lorentzians. b) Left: zero-field spectrum for NV2 with microscopic model fit; Right: spectrum with an applied magnetic field. The fit function is two sets of three Lorentzians. The Lorentzians in each set are separated by the ^{14}N hyperfine splitting. The sets are split from each other by a fit parameter for the ^{13}C hyperfine interaction.

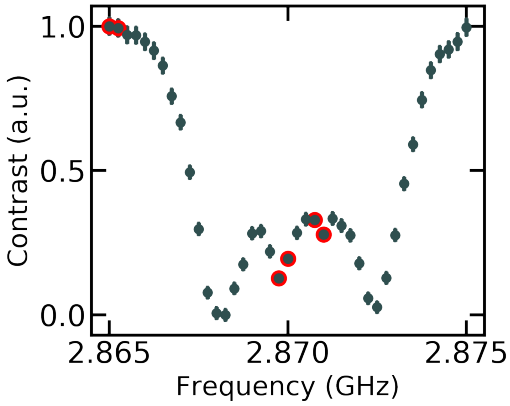

FIG. 9. Position of the six frequencies (red) considered when computing the imbalance. Instead of measuring full-spectra, we take data points closely spaced at the location of each of the two inner resonances and two data points far from the resonances, so as to measure the baseline signal.

to find the positions of the resonances.

4. We generate a spectrum by weighting each resonance by its transition amplitude with the $|m_s = 0\rangle$ state. We compute the wright by fixing the microwave direction in the $\hat{x}$ axis and computing $|\langle 0| S_x |\pm\rangle|^2$.

5. We broaden each resonance by a Lorentzian distribution with full-width-half-maximum of Γ.

6. We use a least-squares regression method on steps 1-5 over the seven fitting parameters, reproducing the

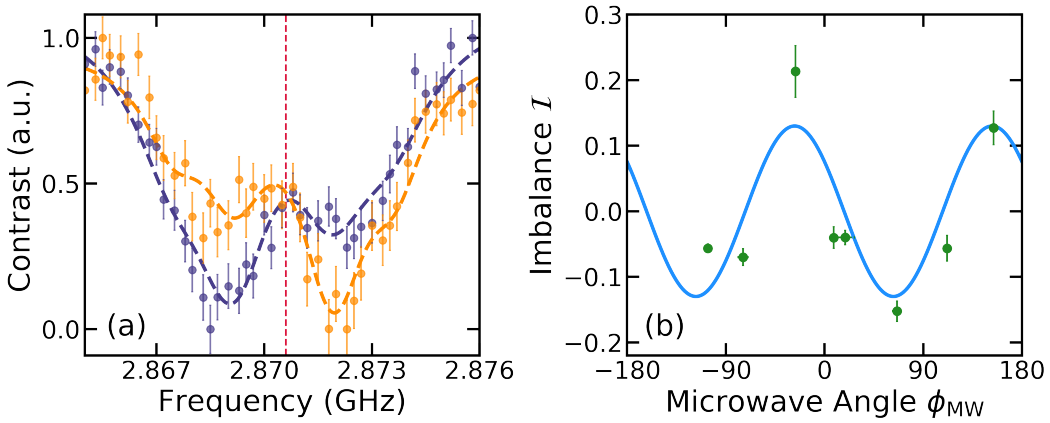

FIG. 10. a) Two spectra from NV2 with fit from the microscopic model at different values of ϕ_{MW}. The dashed vertical line indicates the fit center frequency (2.8706 GHz). We estimate the imbalance by compare the integral on either side of the center frequency. b) Resultant imbalance sinusoid, from where we extract $\phi_E = 236(15)^\circ$.

experimental spectra.

Note, in order to determine Π_z, we use the ensemble-averaged $D_{\mathrm{gs}} = 2870.25(5)$ MHz from the adjacent region of the same diamond containing a high density of NVs as a reference value (Figure 6a).

From the fits (see main text Figure 4a,b) we extract the shifting and splitting due to the electric field:

$$\text{NV1:} \quad \Pi_z = (30 \pm 50)\ \text{kHz} \quad , \quad \Pi_\perp = (650 \pm 10)\ \text{kHz} \tag{18}$$

$$\text{NV2:} \quad \Pi_z = (270 \pm 70)\ \text{kHz} \quad , \quad \Pi_\perp = (850 \pm 80)\ \text{kHz}\ . \tag{19}$$

Using the susceptibilities [3], we extract the electric field vectors at the position of the single NVs:

$$\text{NV1:} \quad (E_x, E_y, E_z) = (-2.1 \pm 0.2,\ \ 3.2 \pm 0.2,\ \ 9 \pm 14)\ \text{MV/m} \tag{20}$$

$$\text{NV2:} \quad (E_x, E_y, E_z) = (-2.8 \pm 1.1,\ \ -4.1 \pm 0.8,\ \ 77 \pm 20)\ \text{MV/m}\ . \tag{21}$$

The parameters of the electric field uniquely determine the position of the positive single fundamental charge (main text Fig. 1b and 1c). The confidence intervals can be estimated using a Monte Carlo method.

---

* These authors contributed equally to this work

[1] S. Whitehead and W. Hackett, Proceedings of the Physical Society **51**, 173 (1939).
[2] B. Smeltzer, L. Childress, and A. Gali, New Journal of Physics **13**, 025021 (2011).
[3] E. V. Oort and M. Glasbeek, Chemical Physics Letters **168**, 529 (1990).